Intermediate-mass black holes: finding of episodic, large-scale, and powerful jet activity in a dwarf galaxy

Monthly Notices of the ROYAL ASTRONOMICAL SOCIETY

MNRAS **520,** 5964–5973 (2023) https://doi.org/10.1093/mnras/stad493
Advance Access publication 2023 February 14

Intermediate-mass black holes: finding of episodic, large-scale, and powerful jet activity in a dwarf galaxy

Jun Yang [1]★ Zsolt Paragi [2] Sándor Frey [3,4,5] Leonid I. Gurvits [2,6] Mai Liao [7,8] Xiang Liu,[9] Lang Cui [9] Xiaolong Yang,[10] Wen Chen [1,11,12] Eskil Varenius [1] John E. Conway,[1] Rurong Chen [13,14] and Ning Chang [9]

[1]*Department of Space, Earth and Environment, Chalmers University of Technology, Onsala Space Observatory, SE-43992 Onsala, Sweden*
[2]*Joint Institute for VLBI ERIC, Oude Hoogevceensedijk 4, NL-7991 PD Dwingeloo, the Netherlands*
[3]*Konkoly Observatory, Research Centre for Astronomy and Earth Sciences, Konkoly Thege Miklós út 15-17, H-1121 Budapest, Hungary*
[4]*CSFK, MTA Centre of Excellence, Konkoly Thege Miklós út 15-17, H-1121 Budapest, Hungary*
[5]*Institute of Physics, ELTE Eötvös Loránd University, Pázmány Péter sétány 1/A, H-1117 Budapest, Hungary*
[6]*Faculty of Aerospace Engineering, Delft University of Technology, Kluyverweg 1, NL-2629 HS Delft, the Netherlands*
[7]*CAS Key Laboratory for Research in Galaxies and Cosmology, Department of Astronomy, University of Science and Technology of China, Hefei, Anhui 230026, China*
[8]*School of Astronomy and Space Sciences, University of Science and Technology of China, Hefei, Anhui 230026, China*
[9]*Xinjiang Astronomical Observatory, Key Laboratory of Radio Astronomy, Chinese Academy of Sciences, 150 Science 1-Street, Urumqi 830011, China*
[10]*Shanghai Astronomical Observatory, Key Laboratory of Radio Astronomy, Chinese Academy of Sciences, Shanghai 200030, China*
[11]*Yunnan Observatories, Chinese Academy of Sciences, Kunming, Yunnan 650216, China*
[12]*University of Chinese Academy of Sciences, No. 19(A) Yuquan Road, Shijingshan District, Beijing 100049, China*
[13]*National Astronomical Observatories, Chinese Academy of Sciences, Beijing 100101, China*
[14]*CAS Key Laboratory of FAST, National Astronomical Observatories, Chinese Academy of Sciences, Beijing 100101, China*

Accepted 2023 February 12. Received 2023 February 10; in original form 2022 November 18

ABSTRACT

Dwarf galaxies are characterized by a very low luminosity and low mass. Because of significant accretion and ejection activity of massive black holes, some dwarf galaxies also host low-luminosity active galactic nuclei (AGNs). In a few dwarf AGNs, very long baseline interferometry (VLBI) observations have found faint non-thermal radio emission. SDSS J090613.77+561015.2 is a dwarf AGN owning an intermediate-mass black hole (IMBH) with a mass of $M_{\rm BH} = 3.6^{+5.9}_{-2.3} \times 10^5 {\rm M}_\odot$ and showing a rarely seen two-component radio structure in its radio nucleus. To further probe their nature, i.e. the IMBH jet activity, we performed additional deep observations with the European VLBI Network (EVN) at 1.66 and 4.99 GHz. We find the more diffuse emission regions and structure details. These new EVN imaging results allow us to reveal a two-sided jet morphology with a size up to about 150 mas (projected length ∼140 pc) and a radio luminosity of about 3×10^{38} erg s^{-1}. The peak feature has an optically thin radio spectrum and thus more likely represents a relatively young ejecta instead of a jet base. The EVN study on SDSS J090613.77+561015.2 demonstrates the existence of episodic, relatively large-scale, and powerful IMBH jet activity in dwarf AGNs. Moreover, we collected a small sample of VLBI-detected dwarf AGNs and investigated their connections with normal AGNs. We notice that these radio sources in the dwarf AGNs tend to have steep spectra and small linear sizes, and possibly represent ejecta from scaled-down episodic jet activity.

Key words: galaxies: active – galaxies: dwarf – galaxies: individual: SDSS J090613.77+561015.2 – radio continuum: galaxies.

1 INTRODUCTION

Relativistic radio jets are frequently found in extragalactic quasars and galaxies (cf. a review by Blandford, Meier & Readhead 2019). For a continuous radio jet (e.g. M87, presented by Walker et al. 2018), the innermost part is referred to as the jet base or the radio core. Because it is partially optically thick at frequencies $\lesssim$10 GHz, it generally shows a relatively flat radio spectra and a very high brightness temperature. Detection of a compact radio core provides strong evidence for the existence of an actively accreting black hole (BH). In case of episodic jet activity, radio cores might be very weak or fully quenched, and only some discrete ejecta are detectable in the images obtained in high-resolution radio interferometric observations of some young radio sources (cf. a recent review by O'Dea & Saikia 2021).

BHs with masses 10^2 M$_\odot \leq M_{\rm BH} \leq 10^6$ M$_\odot$ are usually classified as intermediate-mass black holes (IMBHs). They are expected to be located in low-mass stellar systems: globular clusters (e.g. Wrobel & Nyland 2020; Wrobel et al. 2021) and dwarf galaxies with the stellar

★ E-mail: jun.yang@chalmers.se

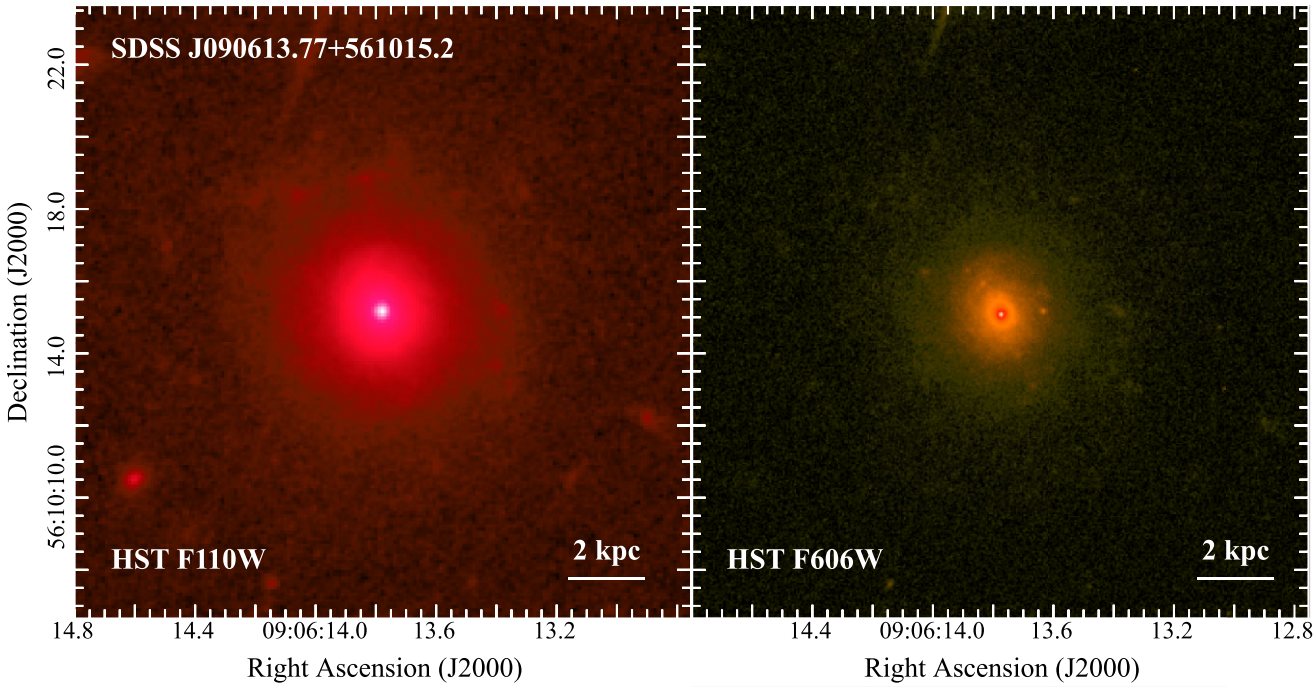

Figure 1. Pseudo-colour images of the dwarf elliptical galaxy SDSS J090613.77+561015.2 observed by the *HST* with its infrared filter F110W and optical filter F606W.

mass $M_\star \leq 10^{9.5}$ $M_\odot$ (cf. reviews by Greene, Strader & Ho 2020; Reines 2022). Many studies at X-ray and infrared wavelengths have been carried out to search for active galactic nucleus (AGN) in dwarf galaxies (e.g. Mezcua & Domínguez Sánchez 2020; Ferré-Mateu, Mezcua & Barrows 2021; Molina et al. 2021; Burke et al. 2022; Salehirad, Reines & Molina 2022). Hunting for IMBHs can help to constrain the BH occupation fraction in dwarf galaxies (e.g. Greene et al. 2020; Haidar et al. 2022), to probe the co-evolution of galaxies and massive BHs (e.g. Greene & Ho 2006, 2007; Kormendy & Ho 2013; Baldassare et al. 2020) and to test theories and computer simulations (e.g. Volonteri 2010; Volonteri et al. 2020; Bellovary et al. 2021; Latif et al. 2022). Moreover, IMBHs may launch continuous or episodic radio jets and outflows, and provide significant feedback to their host galaxies during the AGN phase (e.g. Davis et al. 2022; Koudmani, Sijacki & Smith 2022). Because IMBHs underwent less merging and intensive accretion events throughout their lifetime, their jets might be very faint ($\lesssim$1 mJy) and have significantly different properties (e.g. Liodakis 2022) with respect to those seen in supermassive BHs.

To date, we know little about IMBH jets because of their weakness and low detection rate (e.g. Greene et al. 2020; Reines 2022; Yang et al. 2022a). Some nearby low-mass galaxies have been found to host AGNs likely resulting from accreting IMBHs. High-resolution observations were also performed to search for jets from these promising IMBH candidates: GH 10 (Greene & Ho 2006; Greene, Ho & Ulvestad 2006; Wrobel et al. 2008), POX 52 (Thornton et al. 2008), ESO 243−49 HLX-1 (Webb et al. 2012; Cseh et al. 2015), Mrk 709 (Reines et al. 2014), NGC 205 (M31 satellite, e.g. Lucero & Young 2007; Urquhart et al. 2022), and NGC 404 (Paragi et al. 2014; Nyland et al. 2017; Davis et al. 2020). Very long baseline interferometry (VLBI) observations have also revealed some relatively compact features very likely linked to jet and outflow activity in some sources, e.g. NGC 4395 (Wrobel, Fassnacht & Ho 2001; Wrobel & Ho 2006; Yang et al. 2022a), Henize 2−10 (Ulvestad, Johnson & Neff 2007; Reines & Deller 2012; Nyland et al. 2017; Schutte & Reines 2022), SDSS J090613.77+561015.2 (Yang et al. 2020b), and four low-mass galaxies (Yang et al. 2022b). There are also a few off-centre IMBH candidates reported in a sample of dwarf galaxies with Very Long Baseline Array (VLBA) observations (Reines et al. 2020; Bellovary et al. 2021; Sargent et al. 2022).

Among the known dwarf AGNs, SDSS J090613.77+561015.2 is a potentially interesting target for us to gain more insight into IMBH jets. Fig. 1 displays its faint host galaxy and central bright AGN observed by the *Hubble Space Telescope* (*HST*). It is a dwarf elliptical galaxy with stellar mass $M_\star = 2.3 \times 10^9$ $M_\odot$ (source ID: 9, Reines, Greene & Geha 2013) at the redshift $z = 0.0465$ (scale: 0.94 pc mas^{-1}). Based on high spectral resolution optical observations, Baldassare et al. (2016) estimated the mass of its BH as $M_{\rm BH} = 3.6^{+5.9}_{-2.3} \times 10^5 M_\odot$ (including the systematic uncertainty of 0.42 dex). Its X-ray luminosity is $L_{\rm X} = 4.5 \times 10^{40}$ erg s^{-1} (Baldassare et al. 2017). The existing interferometric observations with the Giant Metrewave Radio Telescope (GMRT) at 150 MHz (Intema et al. 2017) and the Karl G. Jansky Very Large Array (VLA) at $\geq$1.4 GHz (Becker, White & Helfand 1995; Reines et al. 2020; Gültekin et al. 2022) show that its radio counterpart has an optically thin power-law spectrum between 0.15 and 10.65 GHz (Yang et al. 2020b). Its multifrequency radio flux densities are summarized in Table 1. Previous VLBI observations with the European VLBI Network (EVN) show that there are two 1-mJy components with a separation of about 52 mas (Yang et al. 2020b). Based on their slightly elongated structures, relatively high brightness temperatures and the absence of star-forming activity in the host galaxy, the radio morphology very likely results from the IMBH jet activity. Moreover, an integral field spectroscopic study (Liu et al. 2020) and long-slit spectroscopy with the Keck I telescope (Manzano-King, Canalizo & Sales 2019) revealed some spatially extended ionized gas outflows. To further probe the IMBH jet scenario, we carried out deep VLBI observations with the EVN at 1.66 and 4.99 GHz.

Table 1. Total radio flux densities observed for the dwarf AGN SDSS J090613.77+561015.2. A systematic error of 5 per cent is included in the error budget of flux density.

Freq. (GHz)	Flux (mJy)	Array	Reference
0.15	22.4 ± 4.1	GMRT	Intema et al. (2017)
1.40	4.72 ± 0.16	VLA	Becker et al. (1995)
3.00	2.27 ± 0.23	Jansky VLA	Gordon et al. (2021)
6.00	1.44 ± 0.07	Jansky VLA	Gültekin et al. (2022)
9.00	0.93 ± 0.05	Jansky VLA	Reines et al. (2020)
10.65	0.78 ± 0.04	Jansky VLA	Reines et al. (2020)

This paper is organized as follows. We describe our dual-frequency EVN observations and data reduction in Section 2 and present deep EVN imaging results in Section 3. We interpret the observed structure as a consequence of episodic jet activity and discuss some potential implications from a small sample of VLBI-detected dwarf AGNs in Section 4, and give our conclusions in Section 5. Throughout the paper, a standard Lambda cold dark matter cosmological model with $H_0 = 71\ \mathrm{km\,s^{-1}\,Mpc^{-1}}$, $\Omega_m = 0.27$, and $\Omega_\Lambda = 0.73$ is adopted. The spectral index α is defined with the power-law spectrum $S(\nu) \propto \nu^\alpha$, where S is the flux density and ν is the frequency.

2 VLBI OBSERVATIONS AND DATA REDUCTION

We observed SDSS J090613.77+561015.2 at 1.66 and 4.99 GHz with the EVN in 2020 October. Table 2 lists the basic information on the two EVN experiments. The participating telescopes were Jodrell Bank Lovell (JB1) and Mk2 (JB2), Westerbork (WB, single dish), Effelsberg (EF), Medicina (MC), Onsala (O8), Tianma (T6), Urumqi (UR), Toruń (TR), Svetloe (SV), Zelenchukskaya (ZC), Badary (BD), Irbene (IR), Sardinia (SR), Yebes (YS), Kunming (KM), Knockin (KN), Pickmere (PI), and Defford (DE). The telescopes of the enhanced Multi-Element Remotely Linked Interferometry Network (e-MERLIN), KN, PI, and DE were included to provide the short baselines at 1.66 GHz. The EVN stations used the standard experiment set-up: dual circular polarization, 2-bit quantization, 16 sub-bands, 16 MHz per sub-band at 1.66 GHz, and 32 MHz per sub-band at 4.99 GHz. The three e-MERLIN stations used a slightly different set-up: dual circular polarization, 2-bit quantization, two sub-bands, and 64 MHz per sub-band. The observing strategy reported by Yang et al. (2020b) was applied. The source J0854+5757 (Ma et al. 1998) was used as the phase-referencing calibrator. The cycle time for the pair of sources was about 5 min. The data correlations were done by the EVN software correlator (SFXC, Keimpema et al. 2015) at the Joint Institute for VLBI ERIC (JIVE) using standard correlation parameters of continuum experiments: 64 frequency points per sub-band and 1-s integration time.

The visibility data were calibrated using the National Radio Astronomy Observatory (NRAO) Astronomical Image Processing System (version 31DEC21, Greisen 2003) software package. We followed the data calibration recipe reported in Yang et al. (2020b). Because the used 16- and 32-MHz digital filters had a nearly 100 per cent valid bandwidth, we kept all the side-channel data on the baselines to the EVN stations. We flagged out 25 per cent of data on the baselines to the e-MERLIN stations because of the low correlation amplitude at the edge of its 64-MHz digital filter. We noticed some phase jumps on the baselines to IR, and thus excluded these problematic data at 1.66 GHz. Furthermore, we edited out the sub-band data that had a large (∼10 per cent) amplitude scatter because of strong radio frequency interference (RFI) at 1.66 GHz. In the log file of WB, the time stamps of on-source information had a poor accuracy. To flag out these off-source data at the scan beginning, we manually edited the `uvflg` file of WB. Because of RFI, the system temperature data were noisy in particular in the 1.66-GHz experiment. To improve the amplitude calibration, the system temperature data were smoothed using a median filter with a station-dependent time window (1–60 min) long enough to significantly reduce random variation.

We imaged all the sources in the software package DIFMAP (version 2.5e, Shepherd, Pearson & Taylor 1994). The calibrator J0854+5757 had a core–jet structure with integrated flux densities 0.60 ± 0.03 Jy at 1.66 GHz and 0.49 ± 0.03 Jy at 4.99 GHz. The target source SDSS J090613.77+561015.2 was imaged without self-calibration. Before selecting the total intensity (Stokes I) data and doing any data average, we made a small shift (55 mas) to move the peak feature to the image centre in DIFMAP. This helped us to minimize the bandwidth-smearing and time-smearing effects during the later imaging process. After a deep deconvolution with some CLEAN windows covering the potential source region, we noticed some regular noise peaks and strips mainly caused by some small residual errors of the phase-referencing calibration (e.g. Rioja & Dodson 2020). To remove these (faint) noise patterns in the residual map, we flagged out the long-baseline data observed by T6, UR, and BD at elevations $\leq 25^\circ$. This resulted in the more random noise distribution in particular in the on-source region and the change of the map peak brightness from 0.85 to 0.95 mJy beam^{-1} in the 1.66-GHz dirty map made with purely natural weighting. We dropped out the data on the most sensitive baseline EF–JB1 because these data had the highest data weights, suffered strongly from the residual errors, and gave some faint noise peaks (∼0.05 mJy beam^{-1}) in the residual map. Moreover, we excluded the shortest baseline JB1–PI (∼11 km) because of a faint (peak: ∼0.05 mJy beam^{-1}) arcsec-scale strip (possibly resulting from a nearby source in the antenna beam) in the final residual map. To show the centiarcsec-scale structure at 1.66 GHz, we also made a Stokes I map using the data only on the short baselines of <5 million wavelengths (Mλ). At 4.99 GHz, the phase-referencing calibration worked much more accurately for all the stations because of the cleaner receiver band, the higher elevations of the sources, and the smaller residual phase errors resulting from the varying ionosphere.

3 DEEP EVN IMAGING RESULTS

The EVN imaging results of SDSS J090613.77+561015.2 at 1.66 and 4.99 GHz are displayed in Fig. 2. The map parameters

Table 2. Summary of the dual-frequency EVN observations of SDSS J090613.77+561015.2 in 2020 October.

Project code	Starting date and time	Duration (h)	Freq. (GHz)	Data rate (Mbps)	Participating stations
EY035A	2020 Oct 29, 23h30m	6	4.99	2048	JB2, WB, EF, MC, O8, T6, UR, TR, YS, SV, ZC, BD, IR, KM
EY035B	2020 Oct 31, 23h30m	12	1.66	1024	JB1, WB, EF, MC, O8, T6, UR, SV, ZC, BD, IR, SR, KN, PI, DE

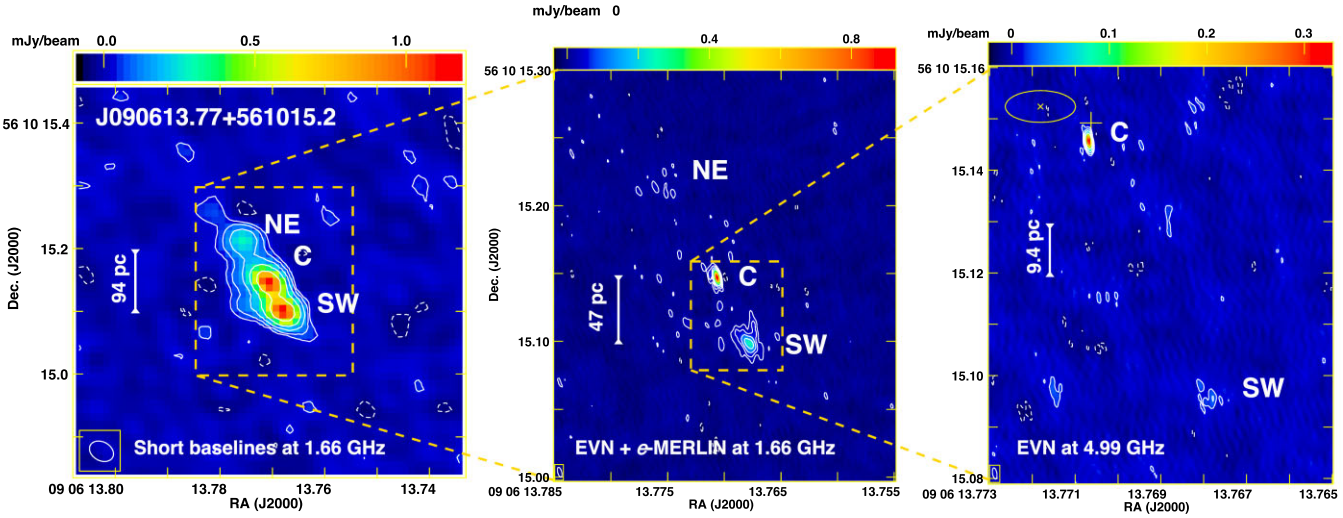

Figure 2. A close look at the radio nucleus of the dwarf galaxy SDSS J090613.77+561015.2. The related VLBI map parameters are listed in Table 3. The synthesized beam is also plotted in the bottom-left corner. Left: The low-resolution total intensity map observed with the EVN plus e-MERLIN at 1.66 GHz and made from the visibility data of $\leq$5 Mλ. Middle: The 1.66-GHz intensity map made from all the data. Right: The high-resolution map observed with the EVN at 4.99 GHz. The accreting IMBH is inferred to be located at the optical centroid. The yellow plus sign marks the *Gaia* DR3 position and the total 1σ error. The yellow cross and ellipse give the Pan-STARRS1 position and the 1σ error.

are listed in Table 3. There are three discrete components detected in the low-resolution map. According to their relative positions, they are labelled as NE, C, and SW. The components C and SW correspond to the components N and S, respectively, in the earlier 1.6-GHz image presented by Yang et al. (2020b) with the phase-referencing observations. The component NE is a new feature and significantly detected with the data on the short baselines in the deep EVN observations at 1.66 GHz. The results of fitting Gaussian brightness distribution models to these components are reported in Table 4. The 1σ formal uncertainties are estimated via adjusting the weight scale to get the reduced $\chi^2_{\rm r} = 1$ in DIFMAP. The last column in Table 4 presents average brightness temperatures, estimated as, e.g. Condon et al. (1982) and Yang et al. (2020b).

The IMBH in the dwarf elliptical galaxy SDSS J090613.77+561015.2 is inferred to be located at the optical centroid (cf. Fig. 1). Table 5 lists the optical coordinates reported by the Panoramic Survey Telescope and Rapid Response System (Pan-STARRS1, Chambers et al. 2016) and the long-term *Gaia* astrometry (Gaia Collaboration 2016, 2022). The errors of the *Gaia* position include the astrometric excess noise (4.2 mas). The large excess noise is mainly caused by the optical nucleus having a faint nuclear disc (likely to be nearly face-on and only clearly visible in the map subtracted the central AGN contribution) and a certain level of asymmetric brightness distribution (Schutte, Reines & Greene 2019).

The radio nucleus displays an elongated structure in Fig. 2. The components NE and SW have a separation of $\sim$130 mas. In the high-resolution EVN maps, the peak component C is also significantly resolved. To accurately characterize its structure, we fit it with an elliptical Gaussian model. At the peak feature, the brightness temperature reaches $(3.5 \pm 1.2) \times 10^8$ K. The component SW shows a clear extension at 1.66 GHz and is only marginally detected at 4.99 GHz. The component NE is a very faint and diffuse feature with a brightness temperature of $(3.9 \pm 0.5) \times 10^5$ K. We fit the components NE (1.66 GHz) and SW (4.99 GHz) with simple circular Gaussian models because of their faintness. There is also more diffuse emission (about 0.8 mJy) that might connect these components and cannot be covered by these Gaussian models in Table 4. To restore this emission, we performed a deep CLEAN. The total flux density of the CLEAN components is $\sim$3.3 mJy at 1.66 GHz. In Table 3, we notice that the low-resolution map did not allow us to restore the more diffuse emission. This is mainly because the short e-MERLIN baselines had a very limited frequency coverage (48 instead of 128 MHz) and the image sensitivity became significantly poorer in particular on the shorter baselines. These missing flux densities ($\sim$16 per cent) might correspond to a larger, resolved structure, e.g. a relic jet, faint mini-lobes, or a radio halo. Future e-MERLIN observations might reveal these potential low surface brightness features.

The radio spectra of SDSS J090613.77+561015.2 between 0.15 and 10.65 GHz are displayed in Fig. 3. The blue data points are from the GMRT observations at 0.15 GHz (Intema et al. 2017), the VLA observations at 1.4 (Becker et al. 1995), 3.0 (Gordon et al. 2021), 6.0 (Gültekin et al. 2022), 9, and 10 GHz (Reines et al. 2020). The blue dashed line plots the best-fitting power-law spectrum, $S(\nu) = (6.1 \pm 0.3)\nu^{-0.84\pm0.03}$, where S in mJy and ν in GHz. The black points give the total flux densities integrated in the high-resolution EVN maps. Because some low surface brightness emission is missed in the EVN maps, there is a certain flux density loss, $\sim$15 per cent at 1.66 GHz and $\sim$64 per cent at 4.99 GHz. Because the e-MERLIN stations were not requested in the 5-GHz experiment, there were no short baselines of $\leq$3.8 Mλ. Thus, there is a large flux density loss at 4.99 GHz. For the very extended structure of the component SW, the direct visibility model fitting recovers the more flux density ($\sim$0.1 mJy) than the CLEAN algorithm. The diffuse component SW can be clearly detected with SNR $\sim$ 8 and slightly higher flux density ($\sim$0.15 mJy) using the data on the short baselines of $\leq$49 Mλ. The image quality is not high enough for us to make a reliable spectral index map between 1.66 and 4.99 GHz to do further studies. The red points plot the flux densities of the peak component C. It has a steep spectrum with $\alpha = -0.87 \pm 0.07$ between 1.66 and 4.99 GHz.

Table 3. Summary of the image parameters in Fig. 2. Columns give (1) panel, (2) maximum baseline length in the (u, v) plane, (3) observing frequency, (4) map RMS noise level, (5) contour levels, (6) peak brightness, (7 and 8) beam size [full width at half-maximum (FWHM)] and major axis position angle, (9) integrated flux density of the CLEAN components, and (10) radio luminosity. The errors in columns (9) and (10) include the systematic errors (5 per cent) because of the limited amplitude calibration accuracy.

Panel	Length	$\nu_{\rm obs}$	RMS	Contours	Peak	Beam FWHM	PA	$S_{\rm int}$	$L_{\rm R}$
	(Mλ)	(GHz)	(mJy beam^{-1})	(× RMS)	(mJy beam^{-1})	(mas × mas)	(°)	(mJy)	(erg s^{-1})
(1)	(2)	(3)	(4)	(5)	(6)	(7)	(8)	(9)	(10)
Left	5	1.66	0.0130	−6, −3, 3, 6, 12, 24, 48	1.150	36.0 × 28.2	65.3	3.32 ± 0.17	(3.0 ± 0.2) × 10^{38}
Middle	49	1.66	0.0070	−6, −3, 3, 6, 12, 24	0.917	7.46 × 2.90	14.9	3.37 ± 0.17	(3.0 ± 0.2) × 10^{38}
Right	154	4.99	0.0043	−6, −3, 3, 6	0.326	2.20 × 0.84	10.0	0.55 ± 0.03	(1.5 ± 0.1) × 10^{38}

Table 4. Summary of the best-fitting elliptical Gaussian models. Columns give (1) component name, (2) observing frequency, (3) signal-to-noise ratio (SNR) in the CLEAN maps, Figs 2(b) and (c), (4) integrated flux density, (5 and 6) relative offsets in right ascension and declination with respect to component N, (7) angular size of the major axis (FWHM), (8) angular size of the minor axis (FWHM), (9) position angle of the major axis for elliptical Gaussians, and (10) brightness temperature. The errors in columns (4) and (10) include the systematic errors (5 per cent) because of the limited amplitude calibration accuracy.

Comp.	$\nu_{\rm obs}$	SNR	$S_{\rm int}$	$\Delta\alpha\cos\delta$	$\Delta\delta$	$\theta_{\rm maj}$	$\theta_{\rm min}$	$\theta_{\rm PA}$	$T_{\rm b}$
	(GHz)		(mJy)	(mas)	(mas)	(mas)	(mas)	(°)	(K)
(1)	(2)	(3)	(4)	(5)	(6)	(7)	(8)	(9)	(10)
NE	1.66	4.9	0.344 ± 0.035	43.03 ± 1.00	65.82 ± 0.09	20.34 ± 1.60	20.34 ± 1.60	–	(3.9 ± 0.5) × 10^5
C	1.66	131.0	1.108 ± 0.055	0.00 ± 0.01	0.00 ± 0.02	1.86 ± 0.11	0.79 ± 0.26	+1.4 ± 3.8	(3.5 ± 1.2) × 10^8
SW	1.66	36.1	1.201 ± 0.060	−23.34 ± 0.13	−47.86 ± 0.11	12.32 ± 0.35	10.44 ± 0.51	+30.9 ± 8.2	(4.3 ± 0.3) × 10^6
C	4.99	76.0	0.424 ± 0.023	0.00 ± 0.01	0.00 ± 0.02	1.03 ± 0.05	0.36 ± 0.13	+2.3 ± 2.0	(6.0 ± 0.2) × 10^6
SW	4.99	6.5	0.246 ± 0.046	−23.47 ± 0.32	−49.55 ± 0.32	6.73 ± 1.00	6.73 ± 1.00	–	(2.9 ± 0.7) × 10^5

Table 5. List of the high-accuracy optical and radio coordinates of the dwarf AGN in SDSS J090613.77+561015.2.

Method	RA(J2000)	$\sigma_{\rm RA}$	Dec.(J2000)	$\sigma_{\rm Dec.}$	Reference
EVN at 5 GHz	$09^{\rm h}06^{\rm m}13\overset{\rm s}{.}770\,69$	$0\overset{\rm s}{.}000\,08$	$+56^\circ10'15\overset{''}{.}1456$	$0\overset{''}{.}0008$	Component C in this paper
Gaia DR3	$09^{\rm h}06^{\rm m}13\overset{\rm s}{.}770\,63$	$0\overset{\rm s}{.}000\,51$	$+56^\circ10'15\overset{''}{.}1492$	$0\overset{''}{.}0042$	Gaia Collaboration (2022)
Pan-STARRS1	$09^{\rm h}06^{\rm m}13\overset{\rm s}{.}771\,81$	$0\overset{\rm s}{.}001\,63$	$+56^\circ10'15\overset{''}{.}1524$	$0\overset{''}{.}0062$	Chambers et al. (2016)

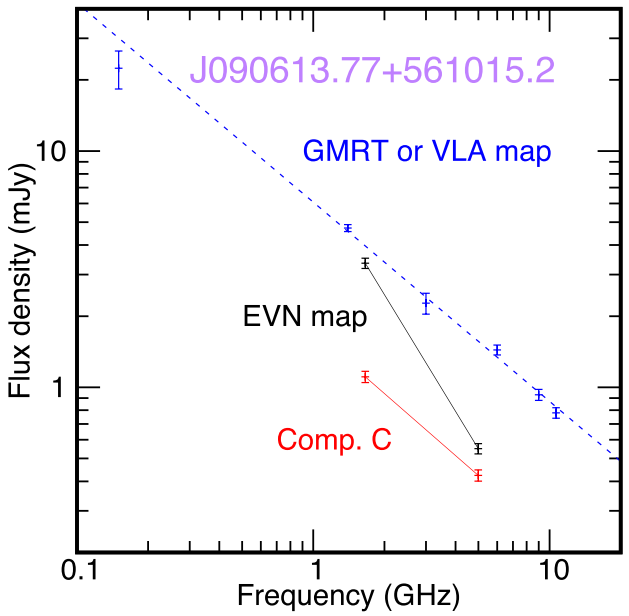

Figure 3. The non-simultaneous radio spectra of SDSS J090613.77+561015.2. The blue points show total flux densities reported in Table 1. The blue dashed line plots their best-fitting power-law spectrum, $S(\nu) = (6.1 \pm 0.3)\nu^{-0.84\pm0.03}$. The black points are total flux densities integrated in the EVN maps. The red points are from the most compact component C.

4 DISCUSSION

4.1 Strong evidence for episodic, large-scale, and powerful IMBH jet activity

The radio structure in SDSS J090613.77+561015.2 has been previously interpreted as a consequence of IMBH jet activity (Yang et al. 2020b). There is no sign of star-forming activity that could be an alternative explanation for radio emission in the dwarf galaxy (Baldassare et al. 2016; Reines et al. 2020). Our new deep EVN images fully confirm the jet interpretation. The detections of the faint component NE and some diffuse emission between the components NE and SW give us a more complete view of the jet structure. To date, it is the first time to get such a fine IMBH jet picture from dwarf AGNs. The jet activity in SDSS J090613.77+561015.2 might have significant impact on the host galaxy and drive kpc-scale high-velocity ionized gas outflows revealed by optical detection of broad [O III] lines (Gelderman & Whittle 1994; Liu et al. 2020; Yang et al. 2020b). The [O III] doublets (4959 and 5007 Å), which contain 80 per cent of the flux of the outflow, reach a width of 1147 ± 5.8 km s^{-1}. This value significantly exceeds the escape velocity (303 ± 35 km s^{-1}) of its halo (Manzano-King et al. 2019). With respect to the optical positions, the jet shows a two-sided structure and may be classified as a compact symmetric object (e.g. Wilkinson, Narayan & Spencer 1994; Kunert-Bajraszewska et al. 2010; An et al. 2012; O'Dea & Saikia 2021).

The component C is a steep-spectrum feature ($\alpha = -0.87 \pm 0.07$ in Fig. 3). With respect to the optical positions provided by the *Gaia*

DR3 (Gaia Collaboration 2022) and Pan-STARRS1 (Chambers et al. 2016) in Table 5, its radio position has no significant offsets. In view of the consistence between optical and radio positions, the more compact structure, and the steep spectrum, we interpret it as a relatively young ejecta (plasma blob) approaching to the Earth. Because of the Doppler deboosting effect, the receding ejecta has very low flux densities ($\leq$0.035 mJy at 1.66 GHz, $\leq$0.022 mJy at 4.99 GHz) and thus is not detected. Assuming that the pair of ejecta were from a symmetric ejection event, we could provide constraints on the jet speed $\beta \geq 0.42c$ and the jet viewing angle $\theta_{\rm v} \leq 65^{\circ}$ with the spectral index $\alpha = -0.84$ (cf. Fig. 3) and the flux density ratio ($\geq$30) between approaching and receding ejecta (e.g. Yang et al. 2020a). Assuming a jet speed close to c, we could provide a limit on the kinematic age of the outer ejecta, $\geq$200 yr. Moreover, SDSS J090613.77+561015.2 is unlikely a very old source because it shows a fairly straight radio spectrum without an electron-cooling break at $\leq$10.65 GHz. If we take the equivalent magnetic field of 3.25 μG for the microwave background, a break frequency of 10–100 GHz, and a magnetic field of 10–1000 μG for the jet, its spectral age will be in the range 10^3–10^7 yr (van der Laan & Perola 1969). If it has a higher break frequency or a higher magnetic field than these assumptions, its spectral age would become younger. The radio spectrum in Fig. 3 shows a hint for the synchrotron self-absorption (SSA) at $\leq$0.15 GHz. Assuming that the SSA is mainly caused by the most compact component C with an angular size of ∼2 mas, and the spectral turnover has a peak frequency of ∼0.1 GHz and a peak flux density of ∼10 mJy, the magnetic field for the inner SSA jet (Kellermann & Pauliny-Toth 1981; O'Dea 1998) would be ∼50 μG. This value is at least one order of magnitude weaker than observed in powerful radio AGNs (e.g. O'Dea 1998; Murgia et al. 1999). Such weak magnetic field would be consistent with a much older spectral age of the jet.

There is no flat-spectrum jet base detected in the EVN maps. The VLBI non-detections do not exclude the existence of a currently accreting IMBH. Because the non-simultaneous radio spectrum in Fig. 3 can be accurately described as a power-law model, the source likely has no strong (>20 per cent) flux density variability over about 25 yr. Moreover, the potential jet base was not seen in the previous EVN observations (Yang et al. 2020b). Thus, the jet base might be intrinsically very weak. Assuming a compact structure, we can provide 5σ upper limits for its flux densities, 0.042 mJy at 1.66 GHz and 0.022 mJy at 4.99 GHz. VLBI non-detections of jet bases are also frequently reported among nearby low-luminosity AGNs (e.g. Fischer et al. 2021) and dwarf AGNs, e.g. $L_{\rm R} \leq 2 \times 10^{33}$ erg s^{-1} for NGC 404 (Paragi et al. 2014) and $L_{\rm R} \leq 5 \times 10^{33}$ erg s^{-1} for NGC 4395 (Yang et al. 2022a). In the radio nucleus of the nearby dwarf starburst galaxy Henize 2−10, there is a pc-scale and low surface brightness component detected with the Long Baseline Array observations (beam FWHM: 0.1 arcsec × 0.03 arcsec) at 1.4 GHz and the VLA observations at 8.5 GHz (Reines & Deller 2012), but fully resolved out with the High Sensitivity Array observations (beam FWHM: 12 mas × 1.9 mas) at 5 GHz (Ulvestad et al. 2007).

The three-component linear structure without a jet base most likely results from multiple major ejection events in SDSS J090613.77+561015.2. The outer components NE and SW are very likely a pair of components launched from the same ejection event. They have a jet opening angle of ∼14° in the sky plane. There also exist some very low surface brightness emissions connecting these components in the 1.66-GHz low-resolution map. The emission might result from the more frequent minor ejection or nearly continuous jet/outflow activity between the major ejection events. Such episodic ejection events were also found during the outbursts

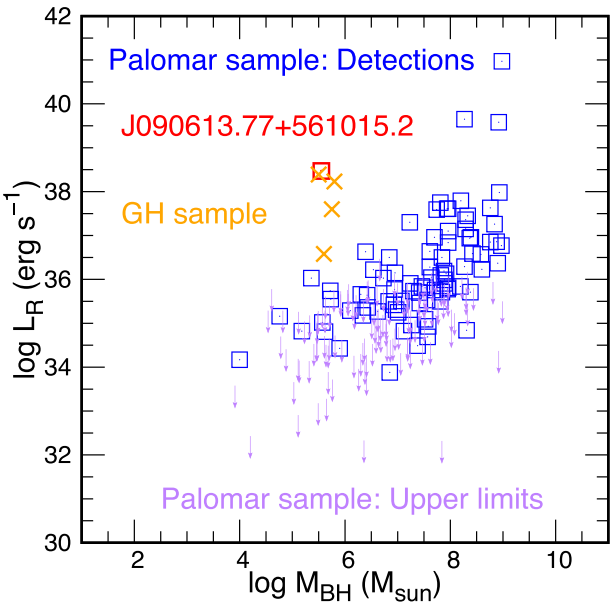

Figure 4. The radio luminosity $L_{\rm R}$ as a function of the BH mass $M_{\rm BH}$ for the pc-scale (candidate) radio cores of the Palomar sample (Ho et al. 1997; Baldi et al. 2021) and some dwarf AGNs. The blue data points refer to optically active and inactive galaxies detected in the e-MERLIN legacy survey at 1.5 GHz (Beswick et al. 2014; Baldi et al. 2021). The dwarf AGN NGC 4395 (e.g. Wrobel & Ho 2006; Yang et al. 2022a) hosting an IMBH with $M_{\rm BH} \sim 10^4$ M$_{\odot}$ (Woo et al. 2019) is also included in the legacy survey and shown as a blue square in the very low mass region. The purple data points refer to 3σ upper limits in the survey. The red point shows our target source SDSS J090613.77+561015.2. The four orange points plot four dwarf AGNs reported by Greene & Ho (2007) and detected by Yang et al. (2022b) with the VLBA at 1.55 GHz.

of Galactic stellar-mass BHs in X-ray binary systems, e.g. XTE J1752−223 (Yang et al. 2010, 2011; Brocksopp et al. 2013), and some extragalactic AGNs, e.g. 3C 120 (Marscher et al. 2002) and NGC 660 (Argo et al. 2015). A knotty jet morphology could also be associated to a more or less continuous jet activity with a certain variation of the jet viewing angle. The more complex explanation includes some significant changes of the Doppler beaming effect along the jet. However, the explanation is not consistent with the relatively stable flux density (cf. Fig. 3) and the non-detection of the jet base near the newly emerging component C.

Among dwarf AGNs hosting (candidate) IMBHs, SDSS J090613.77+561015.2 has a powerful jet with a very high radio luminosity. Fig. 4 displays the radio luminosity $L_{\rm R}$ as a function of the BH mass $M_{\rm BH}$ for the pc-scale candidate radio cores (Baldi et al. 2021) of the Palomar sample (blue and purple points) and some dwarf AGNs (red and orange points). Because of the limited resolution (∼200 mas) of the e-MERLIN, a small fraction of these radio cores might be newly emerging ejecta or star-forming regions in the sample of 280 galaxies. The sample is taken from the optical spectroscopic Palomar survey (Ho, Filippenko & Sargent 1997) and has Dec. > 20°. As an optically selected sample, it has a median distance of 20 Mpc and no significant radio bias. In the plot, we have also added SDSS J090613.77+561015.2 as a red point and four dwarf AGNs detected by Yang et al. (2022b) with the VLBA at 1.55 GHz in the sample of Ho et al. (1997). The four dwarf AGNs show a relatively compact morphology on pc scales and likely represent ejecta from their IMBH jet activity. Compared with the nearby Palomar sample

Table 6. A list of the compact features detected by the VLBI observations in low-mass galaxies. Columns give (1) source name, (2) redshift z, (3) BH mass $M_{\rm BH}$, (4) radio luminosity $L_{\rm R}$ at 1.6 GHz, (5) radio spectral index measured using the VLBI maps for SDSS J090613.77+561015.2 and NGC 4395, and the VLA maps for the rest four sources (Yang et al. 2022b), (6 and 7) projected linear size $D_{\rm LS}$ and angular separation $\theta_{\rm sep}$ estimated from two-sided ejecta for SDSS J090613.77+561015.2 and doubling the offset between VLBI and *Gaia* positions for the rest five sources, (8) brightness temperature of the peak component at 1.4/1.6 GHz, and (9) comment on VLBI structure and reference.

Source Name	z	$\log M_{\rm BH}$	$\log L_{\rm R}$	α	$D_{\rm LS}$	$\theta_{\rm sep}$	$\log T_{\rm B}$	Comment
		($M_\odot$)	(erg s^{-1})		(pc)	(mas)	(K)	
(1)	(2)	(3)	(4)	(5)	(6)	(7)	(8)	(9)
J082443.28+295923.5	0.025	5.6	36.58	−0.63	41.8	41.5	6.9	Faint detection (Yang et al. 2022b)
J090613.77+561015.2	0.046	5.6	38.47	−0.84	123.2	131.4	8.5	Two-sided jet in this paper
J110501.98+594103.5	0.033	5.5	38.39	−1.05	3.3	2.5	7.9	Resolved component (Yang et al. 2022b)
NGC 4395	0.001	4.0	34.38	−0.64	9.2	218.8	6.4	Ejecta or shocks (Yang et al. 2022a)
J131659.37+035319.9	0.045	5.8	38.23	−0.82	343.9	194.1	6.9	Extended feature (Yang et al. 2022b)
J132428.24+044629.6	0.021	5.8	37.60	−0.99	21.6	25.4	6.8	Resolved component (Yang et al. 2022b)

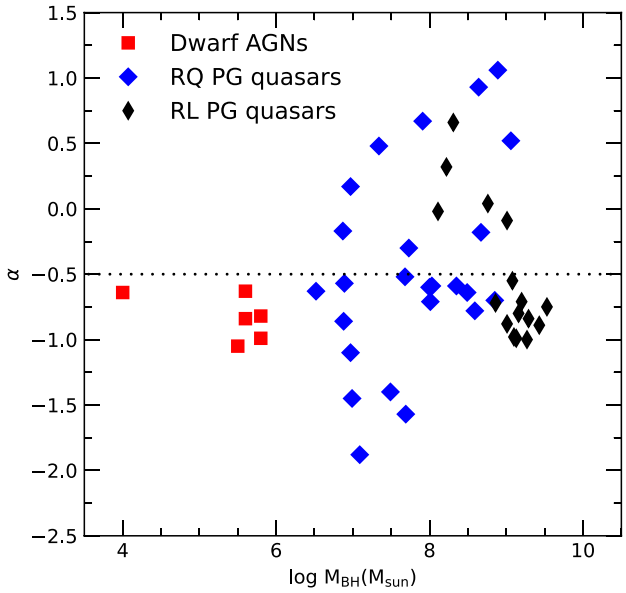

Figure 5. The radio spectral index α versus the BH mass $M_{\rm BH}$ for various radio sources. The red data points show VLBI-detected dwarf AGNs listed in Table 6. They have relatively low radio luminosities, $L_{\rm R}$: $10^{34.4}$–$10^{38.5}$ erg s^{-1}. The blue and black data points represent 25 RQ ($L_{\rm R}$: $10^{38.1}$–$10^{40.6}$ erg s^{-1}) and 16 radio-loud (RL, $L_{\rm R}$: $10^{41.0}$–$10^{44.0}$ erg s^{-1}) sources, respectively, selected by Laor et al. (2019) from the PG quasar sample (Schmidt & Green 1983). The dotted line shows $\alpha = -0.5$. The spectral indices for these PG quasars at redshift $z \leq 0.46$ are measured from non-simultaneous VLA observations between 5 and 8.4 GHz (Laor et al. 2019).

including a few dwarf galaxies, the five dwarf AGNs, in particular SDSS J090613.77+561015.2, have very high radio luminosities. This strongly supports the existence of relatively powerful IMBH jet activity in dwarf AGNs.

4.2 Implications from VLBI-detected dwarf AGNs

There might exist episodic jet activity in other dwarf AGNs as well. Table 6 lists six dwarf AGNs detected in the existing VLBI observations. With respect to the *Gaia* and Pan-STARRS positions, only SDSS J090613.77+561015.2 shows a clearly seen two-sided jet structure. The remaining five sources show a single-component VLBI structure. All the sources have steep spectra between 1.4 and 9 GHz with $-1.1 \leq \alpha \leq -0.6$. Assuming no flux density variability, the spectral indices have an uncertainty of 0.03–0.05 (Yang et al. 2022a, b). The steep spectra observed in these dwarf AGNs were less seen in low-luminosity but more massive AGNs (e.g. Nagar, Wilson & Falcke 2001). Furthermore, these dwarf AGNs have bolometric luminosities $L_{\rm bol} \lesssim 10^{43}$ erg s^{-1} (Yang et al. 2022b) and thus are low-luminosity AGNs (e.g. Ho 2008). Among the population of the low-luminosity AGNs (e.g. Nagar, Falcke & Wilson 2005; Panessa & Giroletti 2013), they have relatively high accretion rates, the Eddington ratio $L_{\rm bol}/L_{\rm Edd} \gtrsim 0.001$ (Baldassare et al. 2017; Yang et al. 2022b), mainly because of their extremely low BH masses. Therefore, these dwarf AGNs appear to be consistent with the broad statistical relation (Laor, Baldi & Behar 2019; Yang et al. 2020c; Chen et al. 2022) stipulating that AGNs with the higher accretion rates have the steeper radio spectra.

Fig. 5 displays the distribution of the radio spectral index α versus the BH mass $M_{\rm BH}$ for the six VLBI-detected dwarf AGNs and the radio sources selected by Laor et al. (2019) from the Palomar–Green (PG) quasar sample (Schmidt & Green 1983). These BH masses have a typical systematic uncertainty of $\sigma \sim 0.4$ dex (Greene & Ho 2007; Davis & Laor 2011). Radio-quiet (RQ) sources with lower BH masses tend to have steep spectra (Laor et al. 2019). Recently, the VLBA observations of RQ PG quasars reveal that they have the more diffuse radio morphology (Wang et al. 2023). This is also in agreement with the the observed steep spectra. Most of these PG quasars have much higher redshifts (z: 0.02–0.46) and radio luminosities ($L_{\rm R}$: 10^{38}–10^{44} erg s^{-1}) than these dwarf AGNs. The VLBI-detected dwarf AGNs also follow the tendency within the regime of 10^4–10^7 $M_\odot$. In view of their steep power-law spectra, high radio luminosities (cf. Fig. 4), and large separations from the optical *Gaia* positions and relatively low brightness temperatures (cf. Table 6), they possibly represent IMBH ejecta or shocks formed by powerful IMBH outflows interacting with surrounding medium (Yang et al. 2022a, b). Future deep VLBI observations similar to those reported here for SDSS J090613.77+561015.2 may clarify the nature of IMBH jet activities.

These VLBI-detected components in the six dwarf AGNs likely represent IMBH ejecta. Based on their angular offsets with respect to the *Gaia* DR3 positions, we derived their projected linear sizes, $D_{\rm LS}$, and reported them in Table 6. This may not be a direct and accurate measurement for each source in the radio image. However, it is meaningful for us to take these measurements for some statistical comparisons with the more massive BHs in AGNs.

High-resolution radio observations of low-BH-mass AGNs could help to probe the speculation that massive BH jets would become more powerful, grow bigger, and live longer after some radio AGN

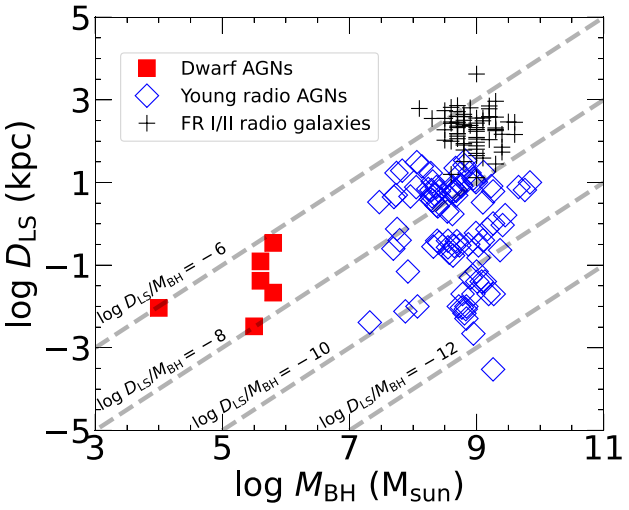

Figure 6. The projected linear size of jets D_{LS} versus the BH mass M_{BH} for young radio sources, FR I/II radio galaxies, and dwarf AGNs. The dashed lines plot some simple power-law functions.

duty cycles because of the co-evolution (Kormendy & Ho 2013; Greene et al. 2020) of BHs and galaxies on cosmic time-scales. Currently, it has been known that the radio luminosity is positively correlated with the BH mass (e.g. Merloni, Heinz & di Matteo 2003; Liodakis et al. 2017). Fig. 6 plots the projected linear size of jets versus the BH mass for the six VLBI-detected dwarf AGNs, some young radio sources (O'Dea 1998; Snellen et al. 2003; de Vries et al. 2009; Cui et al. 2010; Kunert-Bajraszewska et al. 2010; An & Baan 2012; Orienti & Dallacasa 2012), and Fanaroff–Riley (FR) I and II radio galaxies (Black et al. 1992; Nilsson et al. 1993; de Koff et al. 1996; Martel et al. 1999; Harvanek & Stocke 2002; Chandola, Gupta & Saikia 2013). The additional data for the more massive BHs at $z < 4$ were firstly collected by Liao & Gu (2020). These BH masses have an uncertainty of ∼0.5 dex (Liao & Gu 2020). The projected linear sizes are derived from high-resolution VLBI and e-MERLIN imaging results for these powerful young radio sources: compact steep-spectrum sources, high-frequency peakers, GHz-peaked-spectrum radio sources, and compact symmetric objects (e.g. O'Dea 1998; O'Dea & Saikia 2021). The projected linear sizes have much larger ranges, about seven orders of magnitude, and reach ∼1 Mpc for FR I/II radio sources at the high-BH-mass end. The dwarf AGNs are located in the bottom-left corner and significantly extend the range of M_{BH}. However, the low-BH-mass region is still poorly explored. Moreover, faint radio sources at various BH masses are not properly sampled in the plot. Thus, these sources in Fig. 6 cannot be classified as a complete sample.

From the upper envelope of these data points in Fig. 6, there might exist a faint hint for the dependence between the maximum jet length and the BH mass. The upper envelope is significantly less affected by the viewing angles and the ages of the jets, and thus very likely represents intrinsically maximum jet lengths. Because of the small sample size and various sample biases, the upper envelope cannot be accurately characterized. The linear sizes of jets are also correlated with the time-scales of radio AGN duty cycles. Continuous ejection activity on the longer time-scales would help young radio sources develop as large-scale FR I/II radio galaxies (e.g. An et al. 2012; Liao & Gu 2020; O'Dea & Saikia 2021). For rarely seen IMBH jets in dwarf AGNs, they might have significantly low chances to develop as large-scale jets because they suffered less intensive accretion events and had short AGN duty cycle time (e.g. Greene et al. 2020). Host galaxies also have a certain impact on the maximum jet length and may significantly suppress the jet growth in case of a dense surrounding environment (e.g. O'Dea 1998). Moreover, the size measurements are significantly dependent on the observing frequency, sensitivity, and antenna arrays. Generally, high-resolution VLBI observations can detect the radio emission regions with $T_B \gtrsim 10^5$ K, e.g in these dwarf AGNs and young radio sources. Typical interferometric radio observations at <10 GHz have a limited resolution but are much more sensitive to low surface brightness emission regions. This allows us to reveal more kpc-scale FR I/II radio galaxies. If some low-BH-mass sources have very faint jets with $T_B \lesssim 10^5$ K and on sub-kpc scales, they would not be revealed by the current VLBI imaging observations.

In the future, the next-generation VLA (ngVLA[1]) and Square Kilometer Array (SKA[2]) sky surveys would allow us to significantly increase the sample size via the more automatic technique (e.g. machine learning, Bonaldi et al. 2021), in particular towards the low-mass BH side (Liodakis 2022; Lin et al. 2023). The dependence between D_{LS} and M_{BH} would be further investigated.

5 CONCLUSIONS

To search for the direct evidence for a complex IMBH jet activity, we performed deep observations of SDSS J090613.77+561015.2 with the EVN at 1.66 and 4.99 GHz, and revealed more diffuse emission regions and structure details than known previously. These high-sensitivity and high-resolution EVN images clearly display a two-sided and low surface brightness jet morphology extending up to about 150 mas (projected length of ∼140 pc). The IMBH jet has a radio luminosity of 3×10^{38} erg s^{-1} at 1.66 GHz. This is higher than any other candidate IMBH jets in dwarf AGNs. Because the central feature near the optical centroid has an optically thin radio spectrum and an elongated structure, we interpret it as a relatively young ejecta instead of a jet base. Therefore, SDSS J090613.77+561015.2 is the first known case that shows episodic, large-scale, and powerful IMBH jet activity in dwarf AGNs. We also analysed a small sample of VLBI-detected dwarf AGNs. We found that these faint radio sources in dwarf AGNs tend to have steep spectra and compact structures, possibly resulting from scaled-down episodic AGN jet activity.

ACKNOWLEDGEMENTS

We thank the anonymous referee for a very careful and helpful review. The EVN is a joint facility of independent European, African, Asian, and North American radio astronomy institutes. Scientific results from data presented in this publication are derived from the following EVN project code: EY035. e-MERLIN is a National Facility operated by the University of Manchester at Jodrell Bank Observatory on behalf of STFC. This work has made use of data from the European Space Agency (ESA) mission *Gaia* (https://www.cosmos.esa.int/gaia), processed by the *Gaia* Data Processing and Analysis Consortium (DPAC, https://www.cosmos.esa.int/web/gaia/dpac/consortium). Funding for the DPAC has been provided by national institutions, in particular the institutions participating in the *Gaia* Multilateral Agreement. This research has made use of the NASA/IPAC Extragalactic Database (NED), which is operated by the Jet Propulsion Laboratory, California Institute

[1]https://ngvla.nrao.edu/
[2]https://www.skao.int/

of Technology, under contract with the National Aeronautics and Space Administration. This research has made use of NASA's Astrophysics Data System Bibliographic Services. This research has made use of the VizieR catalogue access tool, CDS, Strasbourg, France (DOI: 10.26093/cds/vizier). The original description of the VizieR service was published in 2000, A&AS 143, 23. We thank the staff of the GMRT that made these observations possible. The GMRT is run by the National Centre for Radio Astrophysics of the Tata Institute of Fundamental Research. LC was supported by the National SKA Program of China (No. 2022SKA0120102), the CAS 'Light of West China' Program (No. 2021-XBQNXZ-005), and the National Natural Science Foundation of China (NSFC, grant Nos. U2031212 and 61931002). SF was supported by the Hungarian National Research, Development and Innovation Office (OTKA K134213). WC was supported by the NSFC (grant No. 11903079). XLY thanks the support by the Shanghai Sailing Program (21YF1455300), the NSFC (12103076), and the China Postdoctoral Science Foundation (2021M693267).

DATA AVAILABILITY

The correlation data underlying this article are available in the EVN Data Archive (http://www.jive.nl/select-experiment). The calibrated visibility data underlying this article will be shared on reasonable request to the corresponding author.

REFERENCES

An T., Baan W. A., 2012, ApJ, 760, 77
An T. et al., 2012, ApJS, 198, 5
Argo M. K., van Bemmel I. M., Connolly S. D., Beswick R. J., 2015, MNRAS, 452, 1081
Baldassare V. F. et al., 2016, ApJ, 829, 57
Baldassare V. F., Reines A. E., Gallo E., Greene J. E., 2017, ApJ, 836, 20
Baldassare V. F., Dickey C., Geha M., Reines A. E., 2020, ApJ, 898, L3
Baldi R. D. et al., 2021, MNRAS, 508, 2019
Becker R. H., White R. L., Helfand D. J., 1995, ApJ, 450, 559
Bellovary J. M. et al., 2021, MNRAS, 505, 5129
Beswick R., Argo M. K., Evans R., McHardy I., Williams D. R. A., Westcott J., 2014, in Tarchi A., Giroletti M., Feretti L., eds, Proceedings of the 12th European VLBI Network Symposium and Users Meeting (EVN 2014), Vol. 230, LeMMINGs e-MERLIN Survey of Nearby Galaxies, . Sissa Medialab, Trieste, Italy, p. 10
Black A. R. S., Baum S. A., Leahy J. P., Perley R. A., Riley J. M., Scheuer P. A. G., 1992, MNRAS, 256, 186
Blandford R., Meier D., Readhead A., 2019, ARA&A, 57, 467
Bonaldi A. et al., 2021, MNRAS, 500, 3821
Brocksopp C., Corbel S., Tzioumis A., Broderick J. W., Rodriguez J., Yang J., Fender R. P., Paragi Z., 2013, MNRAS, 432, 931
Burke C. J. et al., 2022, MNRAS, 516, 2736
Chambers K. C. et al., 2016, preprint (arXiv:1612.05560)
Chandola Y., Gupta N., Saikia D. J., 2013, MNRAS, 429, 2380
Chen S. et al., 2022, MNRAS, 512, 471
Condon J. J., Condon M. A., Gisler G., Puschell J. J., 1982, ApJ, 252, 102
Cseh D. et al., 2015, MNRAS, 446, 3268
Cui L., Liu X., Liu J., Song H. G., Ding Z., 2010, A&A, 518, A23
Davis S. W., Laor A., 2011, ApJ, 728, 98
Davis T. A. et al., 2020, MNRAS, 496, 4061
Davis F. et al., 2022, MNRAS, 511, 4109
de Koff S., Baum S. A., Sparks W. B., Biretta J., Golombek D., Macchetto F., McCarthy P., Miley G. K., 1996, ApJS, 107, 621
de Vries N., Snellen I. A. G., Schilizzi R. T., Mack K. H., Kaiser C. R., 2009, A&A, 498, 641
Ferré-Mateu A., Mezcua M., Barrows R. S., 2021, MNRAS, 506, 4702
Fischer T. C. et al., 2021, ApJ, 906, 88
Gaia Collaboration, 2016, A&A, 595, A1
Gaia Collaboration, 2022, preprint (arXiv:2208.00211)
Gelderman R., Whittle M., 1994, ApJS, 91, 491
Gordon Y. A. et al., 2021, ApJS, 255, 30
Greene J. E., Ho L. C., 2006, ApJ, 641, 117
Greene J. E., Ho L. C., 2007, ApJ, 670, 92
Greene J. E., Ho L. C., Ulvestad J. S., 2006, ApJ, 636, 56
Greene J. E., Strader J., Ho L. C., 2020, ARA&A, 58, 257
Greisen E. W., 2003, in Heck A., ed., Astrophysics and Space Science Library, Vol. 285, Information Handling in Astronomy – Historical Vistas. Kluwer, Dordrecht, p. 109
Gültekin K. et al., 2022, MNRAS, 516, 6123
Haidar H. et al., 2022, MNRAS, 514, 4912
Harvanek M., Stocke J. T., 2002, AJ, 124, 1239
Ho L. C., 2008, ARA&A, 46, 475
Ho L. C., Filippenko A. V., Sargent W. L. W., 1997, ApJS, 112, 315
Intema H. T., Jagannathan P., Mooley K. P., Frail D. A., 2017, A&A, 598, A78
Keimpema A. et al., 2015, Exp. Astron., 39, 259
Kellermann K. I., Pauliny-Toth I. I. K., 1981, ARA&A, 19, 373
Kormendy J., Ho L. C., 2013, ARA&A, 51, 511
Koudmani S., Sijacki D., Smith M. C., 2022, MNRAS, 516, 2112
Kunert-Bajraszewska M., Gawroński M. P., Labiano A., Siemiginowska A., 2010, MNRAS, 408, 2261
Laor A., Baldi R. D., Behar E., 2019, MNRAS, 482, 5513
Latif M. A., Whalen D. J., Khochfar S., Herrington N. P., Woods T. E., 2022, Nature, 607, 48
Liao M., Gu M., 2020, MNRAS, 491, 92
Lin J. Y.-Y., Pandya S., Pratap D., Liu X., Carrasco Kind M., Kindratenko V., 2023, MNRAS, 518, 4921
Liodakis I., 2022, MNRAS, 512, 291
Liodakis I. et al., 2017, ApJ, 851, 144
Liu W., Veilleux S., Canalizo G., Rupke D. S. N., Manzano-King C. M., Bohn T., U V., 2020, ApJ, 905, 166
Lucero D. M., Young L. M., 2007, AJ, 134, 2148
Ma C. et al., 1998, AJ, 116, 516
Manzano-King C. M., Canalizo G., Sales L. V., 2019, ApJ, 884, 54
Marscher A. P., Jorstad S. G., Gómez J.-L., Aller M. F., Teräsranta H., Lister M. L., Stirling A. M., 2002, Nature, 417, 625
Martel A. R. et al., 1999, ApJS, 122, 81
Merloni A., Heinz S., di Matteo T., 2003, MNRAS, 345, 1057
Mezcua M., Domínguez Sánchez H., 2020, ApJ, 898, L30
Molina M., Reines A. E., Latimer L. J., Baldassare V., Salehirad S., 2021, ApJ, 922, 155
Murgia M., Fanti C., Fanti R., Gregorini L., Klein U., Mack K. H., Vigotti M., 1999, A&A, 345, 769
Nagar N. M., Wilson A. S., Falcke H., 2001, ApJ, 559, L87
Nagar N. M., Falcke H., Wilson A. S., 2005, A&A, 435, 521
Nilsson K., Valtonen M. J., Kotilainen J., Jaakkola T., 1993, ApJ, 413, 453
Nyland K. et al., 2017, ApJ, 845, 50
O'Dea C. P., 1998, PASP, 110, 493
O'Dea C. P., Saikia D. J., 2021, A&AR, 29, 3
Orienti M., Dallacasa D., 2012, MNRAS, 424, 532
Panessa F., Giroletti M., 2013, MNRAS, 432, 1138
Paragi Z., Frey S., Kaaret P., Cseh D., Overzier R., Kharb P., 2014, ApJ, 791, 2
Reines A. E., 2022, Nat. Astron., 6, 26
Reines A. E., Deller A. T., 2012, ApJ, 750, L24
Reines A. E., Greene J. E., Geha M., 2013, ApJ, 775, 116
Reines A. E., Plotkin R. M., Russell T. D., Mezcua M., Condon J. J., Sivakoff G. R., Johnson K. E., 2014, ApJ, 787, L30
Reines A. E., Condon J. J., Darling J., Greene J. E., 2020, ApJ, 888, 36
Rioja M. J., Dodson R., 2020, A&AR, 28, 6
Salehirad S., Reines A. E., Molina M., 2022, ApJ, 937, 7
Sargent A. J., Johnson M. C., Reines A. E., Secrest N. J., van der Horst A. J., Cigan P. J., Darling J., Greene J. E., 2022, ApJ, 933, 160
Schmidt M., Green R. F., 1983, ApJ, 269, 352
Schutte Z., Reines A. E., 2022, Nature, 601, 329

Schutte Z., Reines A. E., Greene J. E., 2019, ApJ, 887, 245
Shepherd M. C., Pearson T. J., Taylor G. B., 1994, Bull. Am. Astron. Soc., 26, 987
Snellen I. A. G., Lehnert M. D., Bremer M. N., Schilizzi R. T., 2003, MNRAS, 342, 889
Thornton C. E., Barth A. J., Ho L. C., Rutledge R. E., Greene J. E., 2008, ApJ, 686, 892
Ulvestad J. S., Johnson K. E., Neff S. G., 2007, AJ, 133, 1868
Urquhart R., McDermott L. I., Strader J., Seth A. C., Chomiuk L., Neumayer N., Nguyen D. D., Tremou E., 2022, ApJ, 940, 111
van der Laan H., Perola G. C., 1969, A&A, 3, 468
Volonteri M., 2010, A&AR, 18, 279
Volonteri M. et al., 2020, MNRAS, 498, 2219
Walker R. C., Hardee P. E., Davies F. B., Ly C., Junor W., 2018, ApJ, 855, 128
Wang A., An T., Cheng X., Ho L. C., Kellermann K. I., Baan W. A., Yang J., Zhang Y., 2023, MNRAS, 518, 39
Webb N. et al., 2012, Science, 337, 554
Wilkinson P. N., Narayan R., Spencer R. E., 1994, MNRAS, 269, 67
Woo J.-H., Cho H., Gallo E., Hodges-Kluck E., Le H. A. N., Shin J., Son D., Horst J. C., 2019, Nat. Astron., 3, 755
Wrobel J. M., Ho L. C., 2006, ApJ, 646, L95
Wrobel J. M., Nyland K. E., 2020, ApJ, 900, 134
Wrobel J. M., Fassnacht C. D., Ho L. C., 2001, ApJ, 553, L23
Wrobel J. M., Greene J. E., Ho L. C., Ulvestad J. S., 2008, ApJ, 686, 838
Wrobel J. M., Maccarone T. J., Miller-Jones J. C. A., Nyland K. E., 2021, ApJ, 918, 18
Yang J., Brocksopp C., Corbel S., Paragi Z., Tzioumis T., Fender R. P., 2010, MNRAS, 409, L64
Yang J., Paragi Z., Corbel S., Gurvits L. I., Campbell R. M., Brocksopp C., 2011, MNRAS, 418, L25
Yang J., Paragi Z., An T., Baan W. A., Mohan P., Liu X., 2020a, MNRAS, 494, 1744
Yang J., Gurvits L. I., Paragi Z., Frey S., Conway J. E., Liu X., Cui L., 2020b, MNRAS, 495, L71
Yang X. et al., 2020c, ApJ, 904, 200
Yang J. et al., 2022a, MNRAS, 514, 6215
Yang X., Mohan P., Yang J., Ho L. C., Aditya J. N. H. S., Zhang S., Jaiswal S., Yang X., 2022b, ApJ, 941, 43

This paper has been typeset from a TEX/LATEX file prepared by the author.